Peer reviewed version

Link to published version (if available):
10.1021/acsami.0c08174

Link to publication record in Explore Bristol Research
PDF-document

University of Bristol - Explore Bristol Research
General rights

Promoting Active Electronic States in LaFeO₃ Thin-Films Photocathodes via Alkaline-Earth Metal Substitution

Xin Sun, Devendra Tiwari†* and David J. Fermin*

School of Chemistry, University of Bristol, Cantocks Close, Bristol BS8 1 TS, UK

ABSTRACT

The effects of alkaline-earth metal cation (AMC: Mg^{2+}, Ca^{2+}, Sr^{2+} and Ba^{2+}) substitution on the photoelectrochemical properties of phase-pure LaFeO₃ (LFO) thin-films are elucidated by X-ray Photoemission Spectroscopy (XPS), X-ray Diffraction (XRD), diffuse reflectance and electrochemical impedance spectroscopy (EIS). XRD confirms the formation of single-phase cubic LFO thin films, with a rather complex dependence on the nature of the AMC and extent of substitution. Interestingly, subtle trends in lattice constant variations observed in XRD are closely correlated with shifts in the binding energies of Fe $2p_{3/2}$ and O 1s orbitals associated with the perovskite lattice. We establish a scaling factor between these two photoemission peaks, unveiling key correlation between Fe oxidation state and Fe-O covalency. Diffuse reflectance shows that optical transitions are little affected by AMC substitution below 10%, which are dominated by a direct bandgap transition close to 2.72 eV. Differential capacitance data obtained from EIS confirm the p-type characteristic of pristine LFO thin-films, revealing the presence of sub-bandgap electronic state (A-states) close to the valence band edge. The density of A-states is decreased upon AMC substitution, while the overall capacitance increases (increase in dopant level) and the apparent flat-band potential shifts towards more positive potentials. This behaviour is consistent with the change in the valence band photoemission edge. In addition, capacitance data of cation-substituted films show the emergence of deeper states centred around 0.6 eV above the valence band edge (B-states). Photoelectrochemical responses towards the hydrogen evolution and oxygen reduction reactions in alkaline solutions show a complex dependence on alkaline-earth metal incorporation, reaching incident-photon-to-current conversion efficiency close to 20% in oxygen saturated solutions. We rationalise the photoresponses of the LFO films in terms of the effect sub-bandgap states on majority carrier mobility, charge transfer and recombination kinetics.

Keywords: LaFeO₃ thin-films, photocathodes, Alkaline-earth metal cations, lattice substitution, oxygen photoreduction, surface states

INTRODUCTION

Transition metal oxide absorbers have attracted widespread attention in fields such as water-remediation, water-splitting and photovoltaic devices, primarily due to their chemical stability and tunability of electronic properties.[1,2] Efforts have been devoted primarily to oxide photoanodes, such as TiO_2,[3] Fe_2O_3,[4,5] and $BiVO_4$,[6–8] which exhibit excellent chemical stability but poor light-harvesting, very short carrier-lifetime and fast surface recombination rate in comparison to the oxygen evolution reaction. On the other hand, significantly less is known about transition metal oxide photocathodes. Copper-based electrodes such as Cu_2O,[9] and $CuBi_2O_4$[10,11] show attractive external quantum efficiency (EQE) for hydrogen evolution (HER), but chemical stability remains a significant challenge. Current strategies, including coating a protective layer (e.g. TiO_2) onto semiconductor surfaces and metal doping have extended their lifetime under operational conditions.[10,12–14] On the other hand, ferrite materials including $LaFeO_3$,[15–17] $YFeO_3$,[18] $BiFeO_3$,[19] $PrFeO_3$,[20] $CuFeO_2$,[21] and $CaFe_2O_4$[22] are chemically stable, but their EQE values are significantly lower.

LaFeO$_3$ (LFO) is a p-type semiconductor exhibiting high photovoltages towards the HER, but low EQE values, regardless of the synthesis methods.[15–17,23,24] In a recent publication, we identify that EQE can be substantially enhanced by depositing a thin TiO_2 film which acts as a hole-blocking layer at the LFO/water interface.[15] EQE enhancement has also been reported by depositing a thin Au interlayer between the FTO and LFO films.[25] Metal cation substitution has also been put forward as a potential strategy to improve photoelectrochemical responses. Wheeler et al. reported an increase in photoelectrochemical responses upon 3% K^+ substitution at the A-site, which was primarily linked to changes in the light capture cross-section.[26] Substitution by Mg^{2+} and Zn^{2+} has also shown improvement in photocurrent responses,[27] although it remains to be fully elucidated which sites are being replaced and how these affect the electronic properties of LFO.

In this study, we uncover complex trends in the photoelectrochemical responses of thin LFO films upon alkaline-earth metal cation (AMC: Mg^{2+}, Ca^{2+}, Sr^{2+} and Ba^{2+}) substitution of up to 10%. The AMCs are introduced in the sol-gel precursor, keeping the Fe(III) precursor concentration constant. XRD shows a complex dependence of the lattice constant with the type and extent of AMC substitution. Interestingly, the Fe $2p_{3/2}$ and O 1s binding energies extracted from quantitative XPS analysis show a qualitatively similar compositional dependence, revealing a direct correlation between Fe oxidation state and Fe-O covalency. Electrochemical Impedance Spectroscopy (EIS) unveils the presence of sub-bandgap states generated upon AMC substitution, which play key roles in the kinetics of photoelectrochemical oxygen and water reduction reactions, surface recombination kinetics and dynamics of majority carrier transport.

EXPERIMENTAL

Thin-film preparation. All chemicals were purchased commercially with the highest purity available. Solutions were prepared with ultrapure Milli-Q water (18 MΩ resistance). Thin films were deposited using sol-gel methods in the presence of citric acid as a chelating agent.[21,27] La(NO$_3$)$_3$·6H$_2$O (0.116 M), Fe(NO$_3$)$_3$·9H$_2$O (0.116 M) and citric acid (0.232 M) were dissolved into 4.3 mL water and ethanol (5:4) and stirred for 2 hours, forming a clear solution. Ethylene glycol (0.06mL) was added into the mixture and further stirred for 20 hours. The solution was spin-coated onto F: doped SnO$_2$ (FTO) substrates with a rotation speed of 3000 rpm for 30 seconds. The film was dried at 100 °C for 10 minutes, followed by heating to 400 °C for 1 hour. Subsequently, the same procedure was repeated three times to generate thin-films with a thickness of approximately 95 nm. The films were finally calcined at 600 °C

for 3 hours. In the case of AMC thin-films, the La^{3+} precursor was stoichiometrically substituted with either $Mg(NO_3)_2 \cdot 6H_2O$, $Ca(NO_3)_2 \cdot 4H_2O$, $Sr(NO_3)_2$ and $Ba(NO_3)_2$, keeping the concentration of Fe precursor and citric acid constant. SEM images in **Figure S1a** (Supporting Information) show no specific morphological features upon AMC substitution, while the film morphology is dominated by the F-doped SnO_2 (FTO). EDX Energy-dispersive X-ray (EDX) analysis (**Figure S1b**) confirms that the AMC content in the films is very close to the composition in the sol-gel precursor.

Instrumentation. Powder XRD was recorded with a Bruker AXS D8 Advance diffractometer using a Ni-filtered Cu-Kα source (λ = 1.54016 Å). Thin-film morphology and composition were analysed by scanning electron microscopy (SEM, Jeol iT300) and with energy-dispersive X-rays analysis – EDX (Oxford Xmax-80 detector coupled to SEM), respectively. Diffuse-reflectance data in the visible range was measured with a Shimadzu UV-2600 spectrophotometer. Photoelectrochemical experiments were performed in 0.1 M Na_2SO_4 pH 12 solution, with an Ivium Compactstat potentiostat, employing a glassy carbon counter-electrode and Ag/AgCl (KCl saturated) reference electrode. Photocurrent transient measurements were measured with a 405 nm LEDs (Thorlabs) driven by a waveform generator (Stanford Research Systems). Measurement of external quantum efficiency (EQE) spectra was performed by a 100 W quartz halogen lamp (Bentham ILD-D2-QH) and a monochromator (Bentham TMc 300). Photon flux was referenced against a Si photodiode (Newport corporation, NREL calibrated). The electrolytes were Ar-purged or O_2-purged 0.1 M Na_2SO_4 pH 12 aqueous solutions. All potentials are referred to against the reversible hydrogen electrode (RHE). Electrochemical Impedance Spectra (EIS) were recorded with Modulab potentiostat and frequency response analyser with 13 mV RMS amplitude of modulation between 1.7 Hz and 11.7 kHz. The X-ray photoelectron spectroscopy of as-received $LaFeO_3$ samples was carried out at the Bristol NanoESCA Facility. The spectra were acquired employing an excitation from a non-monochromatic Al Kα line in a chamber with a base pressure of 4×10^{-11} mbar. The emitted photoelectrons are analysed with an ARGUS spectrometer with an overall energy resolution of 0.9 eV. The detail scans of the core levels and survey scans are collected with pass energies 20 eV and 50 eV, respectively. Charge-correction was performed against the adventitious C 1s peak assumed at 284.8 eV. The deconvolution of the core bands is done using Gaussian-Lorentzian composite functions after Shirley background subtraction using XPSPEAK code.

RESULTS AND DISCUSSION

Thin-film structure and optical properties. Figure 1 illustrates XRD patterns of pristine and AMC substituted LFO thin films deposited onto glass. **Figure 1a** contrasts the pristine and 3% Ba^{2+} substituted LFO films, exhibiting the pattern associated with the *pm-3m* cubic phase. **Figure S2** (supporting information) shows the XRD patterns of the pristine LFO and 7% AMC substituted films refined to the JCPDS-ICDD database file 01-075-0541, confirming the phase purity of the thin films. **Figure 1b** focuses on the position of the (110) diffraction peak for 7% substituted LFO, revealing that the extent of lattice distortion depends on the nature of AMC. The complex dependence of the diffraction angle with the extent of Ba^{2+} substitution is illustrated in **Figure 1c**, where an initial shift toward slightly higher 2θ values is then reversed to values closer to the pristine LFO.

The evolution of the structural parameters upon AMC substitution were investigated by Pawley refinement of the XRD pattern as described in **Figure S2**. The analysis shows a decrease in the lattice constant by approximately 2 pm upon 7% AMC substitution, although the absolute values should be considered cautiously given the broadening induced by the small crystalline domains (less than 100 nm). This is an interesting trend considering, for example, that the lattice constant of the cubic $BaFeO_3$ is reported as 3.971 Å.[28] We rationalise this behaviour in terms of the promotion of

higher Fe oxidation states, which feature smaller ionic radius, as a result of charge compensation upon La^{3+} substitution by the divalent AMC. Although Sr^{2+} and Ba^{2+} have larger ionic radius than La^{3+}, the net change in the unit-cell size is dominated by the decrease in the Fe ionic radius at this low substitution levels. The trend in **Figure 1c** shows that as Ba^{2+} substitution increases over 5%, the shrinking in lattice constant induced by the higher oxidation state in the B-site is partially compensated by the larger A-site cation. Although the behaviour observed in the XRD upon AMC substitution is highly reproducible, comparison with previous studies should be considered cautiously. Aspects such as nanocrystalline domain size, temperature and substrate induce strain can all play a role in the trends observed.
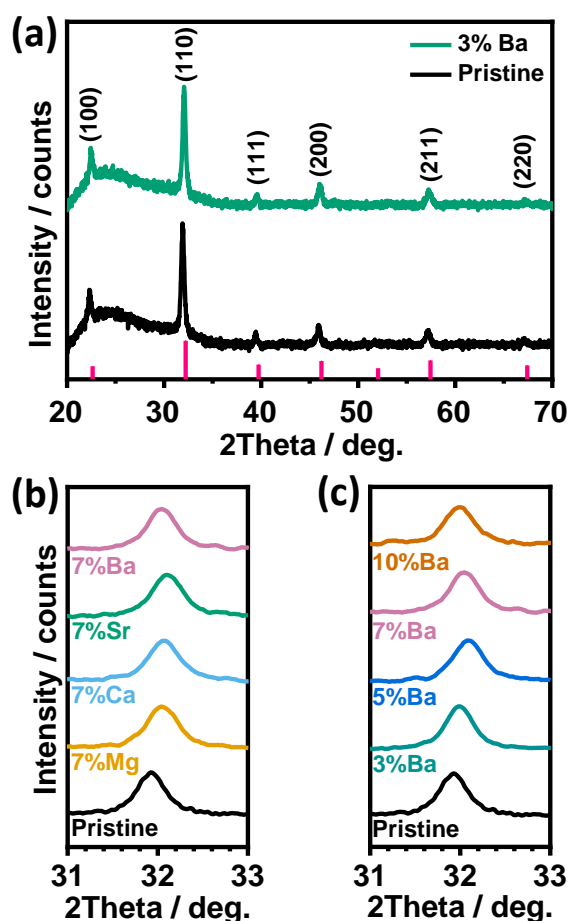

Figure 1. XRD of alkaline-earth metal cation (AMC) substituted $LaFeO_3$ (LFO) thin-films: (a) XRD patterns of pristine and 7% Ba^{2+} substituted LFO thin films, along with Bragg reflections (pink bars) from the JCPDS-ICSD standard 01-075-0541, showing the key features associated with the *pm-3m* cubic phase. (b) Evolution of the (110) peak upon 7% substitution of the various AMC and (c) as a function of the extent of Ba^{2+} substitution.

Semi-Quantitative XPS analysis was carried out across the whole range of AMC substituted LFO thin-films, with representative deconvolutions of the La 3d, Fe 2p and O 1s photoemission bands shown in **Figure S3** (Supporting Information). The La 3d region contains two photoemission peaks with binding energies (BE) at 833.9 and 850.9 eV associated with La $3d_{5/2}$ and La $3d_{3/2}$, respectively.[29–31] These peak positions confirm the La^{3+} oxidation state, which is also supported by the 17 eV spin-orbit component separation between the doublet. Three different components were presented in the deconvolution of the O 1s peak, with the lowest BE (529.2 eV) linked to oxygen in the perovskite lattice,

and the other two components assigned to hydroxyl group and carbonated species.[29] The predominant Fe^{3+} oxidation state can be described by the peak positions of Fe $2p_{3/2}$ at around 709.6-710.6 eV and Fe $2p_{1/2}$ at 722.8-724.2 eV, with a spin-orbit splitting of around 13.6 eV and satellite peaks at approximately +8.6 eV from each doublet. The deconvolution of the broad Fe 2p photoemission is not straightforward given the complexity introduced by multiple-splitting, multiple oxidation states and charge transfer effects.[32–34] In this study, we have implemented a simple approximation based on previous photoemission studies of Fe oxides, supported by highly sensitive Mossbauer spectroscopy.[35,36] The Fe 2p peak can be deconvoluted into three components, with the most prominent being assigned to Fe^{3+} species. The smaller peaks at higher binding energies correspond to higher iron oxidation states, with some studies linking these features to Fe^{4+},[26,35–38] although this would require systematic analysis of other Fe core levels.[39]

Figure 2 displays the dependence of the binding energies of Fe $2p_{3/2}$ and O 1s orbitals associated with the perovskite lattice as a function of AMC substitution (7%), as well as various Ba^{2+} substitution levels. The BEs of Fe $2p_{3/2}$ and O 1s show similar non-monotonic trends to those observed in the (110) XRD peak upon AMC substitution (**Figure 1**). This remarkable observation suggests that the interplay between changes in Fe site oxidation state and lattice distortion introduced by the AMC substitution affects the surface electronic structure of the thin-film.
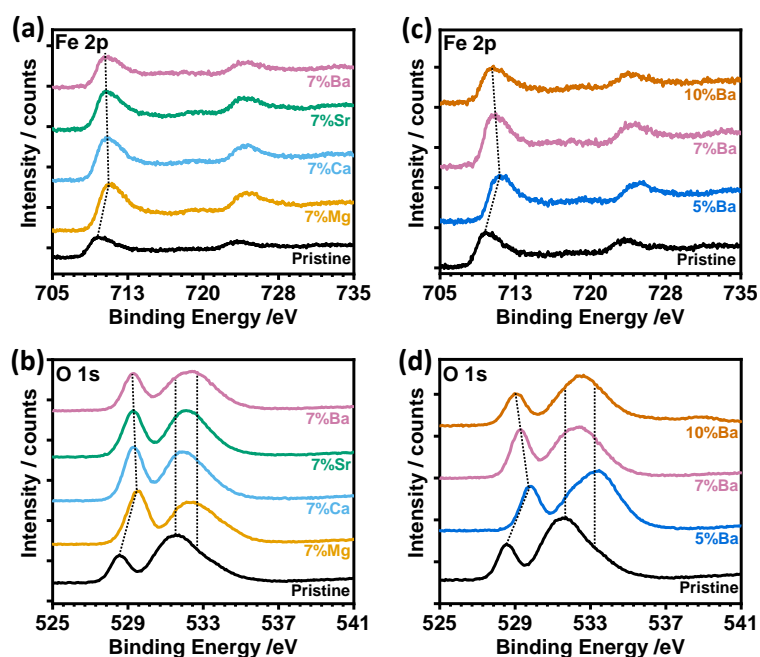

Figure 2. Evolution of the XPS spectra in the regions of Fe 2p (a,c) and O 1s (b,d) upon 7% AMC substitution and extent of Ba^{2+} substitution. Deconvolution analysis of the XPS features is exemplified in **Figure S3**.

The scaling relation between Fe oxidation state and bond covalency is displayed by the linear correlation between Fe $2p_{3/2}$ and O 1s binding energies in **Figure 3**. This trend shows that the increase in the oxidation state of Fe sites promoted by AMC substitution manifests itself by a shift of the Fe $2p_{3/2}$ peak towards higher BE, a subtle decrease in the perovskite lattice constant and an increase in the degree of covalency, which in turns drives the O 1s binding energy towards higher values. No such correlation is observed between O 1s and La 3d. The thin-film nature of our material, as well as the

processing temperatures used, may also play a role in the trends observed, although Shen et al.[40] have also postulated that Fe^{4+} sites can lead to a stronger Fe-O bond.
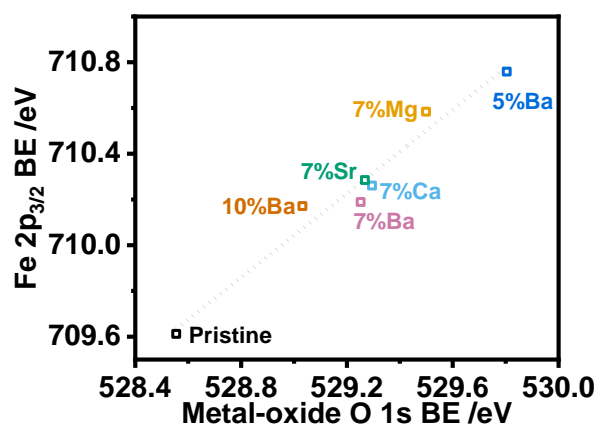
Figure 3. Correlation between binding energies (BEs) of Fe 2p$_{3/2}$ and O 1s (perovskite lattice) in pristine and AMC substituted LFO films. This trend strongly suggests that Fe oxidation state and covalency of the Fe-O bond are strongly correlated.
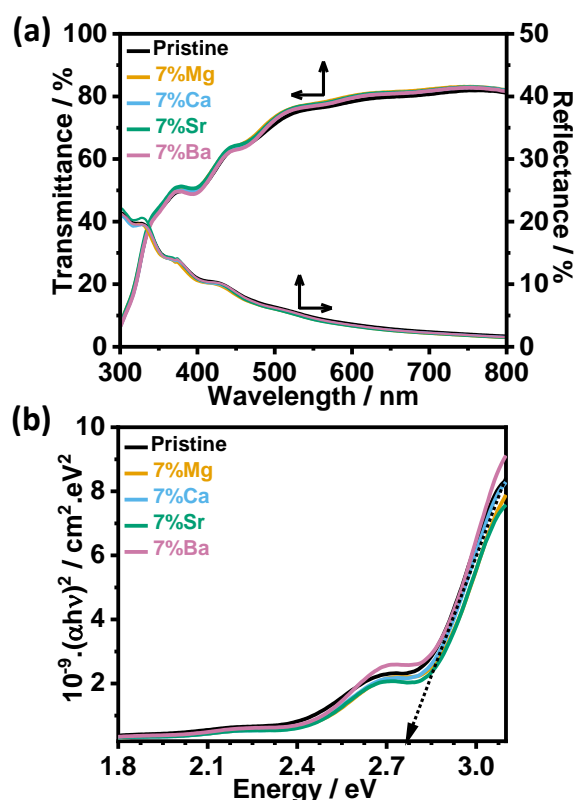
Figure 4. Optical properties of 95 nm pristine and 7% AMC substituted LFO thin films: (a) transmittance and reflectance spectra in the visible range; (b) Tauc plots showing the main absorption edge at 2.72 eV.

Diffuse reflectance spectra shown in **Figure 4a** reveal that AMC substitution up to 7% has minimal effect in the optical properties of LFO. The data clearly shows that AMC substitution, in the

concentration range investigated, have little influence on the optical properties of the thin-film. Furthermore, the virtually identical values demonstrate the reproducibility of our deposition method in terms of thickness and film morphology, which strongly affect the film optical parameters. Tauc plots in **Figure 4b** shows the optical bandgap energy of pristine and all AMC substituted films are all close to 2.72 eV. LFO shows two distinctive sub-bandgap transitions which do not generate free charge carriers.[15] It should be mentioned that Wheeler et al. reported more substantial changes in the optical properties upon 3% K^+ substitution.[26] We have also observed spectral changes at AMC substituted LFO powders processed at temperatures above 800 ˚C.

Photoelectrochemical responses. Cyclic voltammograms of pristine and 7% AMC substituted LFO films in 0.1 M Na_2SO_4 pH 12 in the dark are displayed in **Figure 5a**. The voltammograms, recorded at 100 mV s^{-1}, show an increase in the capacitive current in the range of 0.4 to 1.5 V vs RHE with respect to the pristine LFO films. The onset of oxygen evolution can be seen at potentials beyond 1.4 V, indicating the transition from reverse to forward bias. A broad pseudo-capacitive feature can be seen at potentials around 1.3 V in the case of pristine LFO while a more significant response can be seen at less positive potential upon 7% AMC substitution. **Figure 5b** shows that the pseudo-capacitive response between 0.8 and 1.0 V increases upon the increasing concentration of Ba^{2+} in the film. Plots of differential capacitance as a function of the applied potential in **Figure 5c** further emphasise the trends observed in cyclic voltammetry. Each capacitance point shown in **Figure 5c** was calculated from electrochemical impedance spectra as described in Experimental. Indeed, AMC substitution promotes a significant increase in the capacitance across the whole potential range, suggesting a significant increase in the density of acceptor states (doping density). We also see an increase in the capacitance of the pristine LFO films from 1.2 eV and a prominent shoulder at 1.4 eV, which are linked to sub-bandgap surface states (A-states). The transition from reverse to forward bias in the AMC substituted films occurs about 0.2 V more positive than in the pristine LFO films, with a broad pseudo-capacitive feature in the range of 0.8 to 1.1 eV (B-states) depending on the AMC. The data in **Figure 5** clearly show that the density of B-states depends on the extent of AMC substitution, while A-states appears to dampen by all AMC substantially.

Based on the link between the emergence of B-states and AMC substitution, these states are likely to involve a combination of Fe 3d and O 1s states as a result of the presence of higher Fe oxidation states.[26,41] On the other hand, A-states are linked to intrinsic defects which tend to generate states closer to the valence band edge. Indeed, Taylor et al. concluded that Schottky disorder compensated by cation vacancies could generate intrinsic sub-bandgap states near the valence band.[42] In principle, the position of these states probed by electrochemical methods can be strongly influenced by the hydration energy.[43] Consequently, we could have a rather complex picture in which these states may have different energies in bulk and at the surface. Further below, we will demonstrate that these states have a strong effect on the photoelectrochemical responses of LFO films.
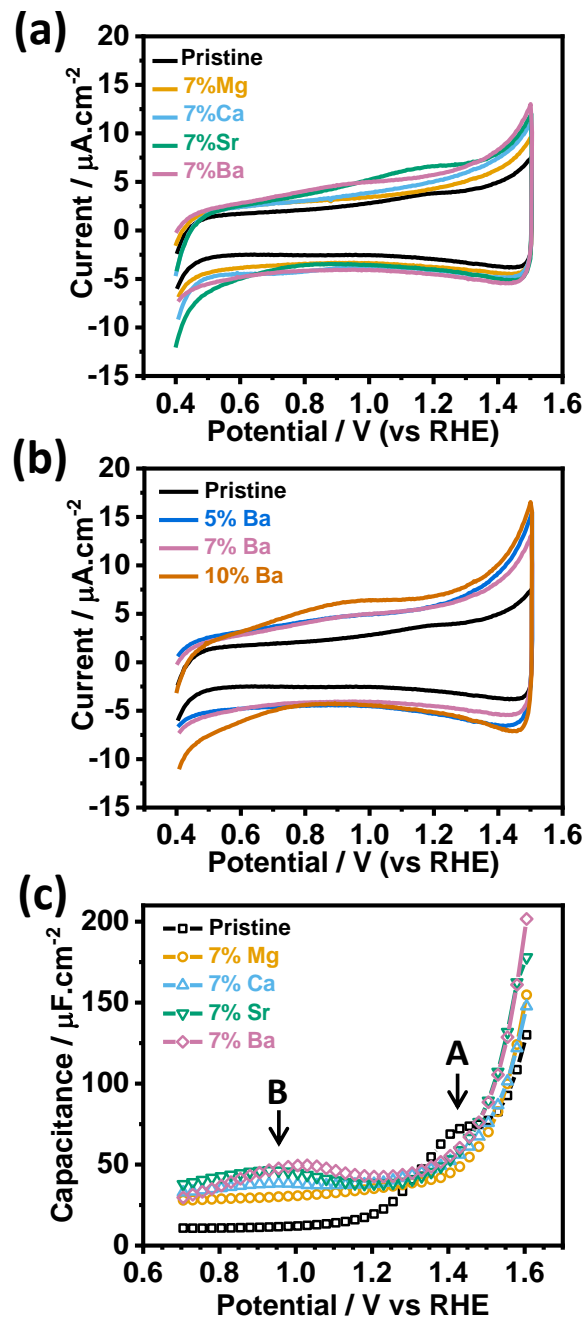
Figure 5. Electrochemical responses in 0.1 M Na$_2$SO$_4$ pH 12: (a) cyclic voltammograms of pristine and 7% AMC substituted LFO films at 0.1 V s^{-1}; (b) cyclic voltammograms as a function of the Ba^{2+} substitution extent at 0.1 V s^{-1}; (c) Capacitance voltage curves extracted from electrochemical impedance spectra of pristine and 7% AMC substituted films, highlighting the pseudo-capacitive elements associated with A and B sub-bandgap states
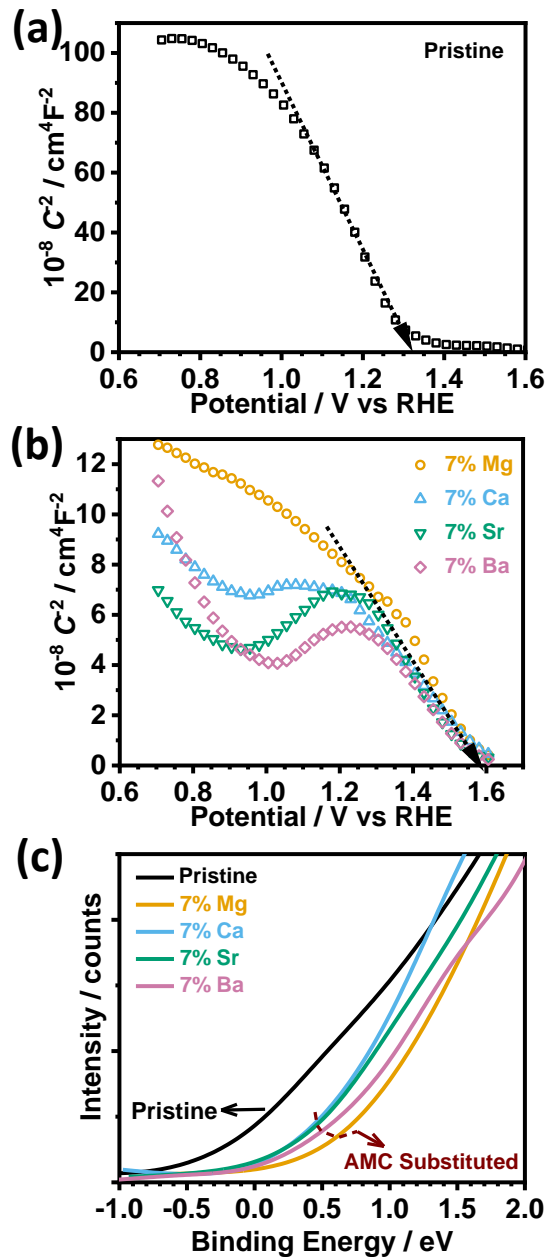
Figure 6. Valence band edge position: (a-b) Mott-Schottky plots of the pristine and 7% AMC substituted LFO films in 0.1 M Na_2SO_4 pH 12; (c) valence band edge calculated from XPS analysis of the pristine and AMC substituted films. Both approaches appear to show a valence band edge shift of approximately 300 meV upon AMC substitution.

Mott-Schottky plots of the pristine and the 7% AMC substituted LFO films are displayed in **Figures 6**. The presence of A and B states introduces significant complexity and uncertainty in the analysis of these plots. From the linear segment of the pristine LFO plot, a flat band potential (U_{fb}) of 1.32 V vs RHE, although this value would be affected by Fermi-level pinning (FLP) induced by the A-states (**Figure 6a**). On the other hand, FLP at B-states substantially distorts the Mott-Schottky plots up to 1.2 V. Extrapolating from this potential onwards; **Figure 6b** suggest a U_{fb} = 1.58 V vs RHE regardless of the type and extent of AMC substitution. Interestingly, **Figure 6c** contrasts the valence band edges of the LFO films (pristine and 7% AMC substituted) estimated from XPS spectra. The valence band

onset of the AMC substituted films are all shifted by approximately 300 meV with respect to the pristine films, further confirming the lowering of the Fermi energy upon AMC substitution.

Figure 6c also shows a sharper increase in photoemission intensity at the valence band edge of the AMC substituted with respect to the pristine film. Based on the Fermi-Dirac Distribution, this trend suggests an increase in acceptor states (conductivity) upon AMC substitution. A similar trend can be extracted from the Mott-Schottky analysis (**Figures 6a** and **6b**), although quantification of the majority carrier density is rather complex due to the FLP induced by the surface states and the acute dependence of the relative permittivity on parameters such as grain size and annealing temperature.[44] A rough estimation based on the linear portions highlighted in **Figure 6a** and **6b**, suggest that pristine LFO would be in the range of 2.3×10^{17} cm^{-3}. At the same time, AMC substituted LFO in the range investigated is approximately 10 times larger. This observation is also consistent with the strong dependence of LFO conductivity on the extent of Sr^{2+} substitution reported by Shen et al.[40] On the other hand, the valence band spectrum of the pristine LFO appears to show a higher density of states at E_f. We link this density of states to the sub-bandgap A-states which are not well resolved in the energy scale due to the small cross-section of these states under the X-ray excitation used. Thus, a consistent picture of the density of states near the valence band edge is emerging from the differential capacitance-voltage curve (**Figure 5c**) and the valence band spectra (**Figure 6c**).

Figure 7a and **7b** show linear sweep voltammograms (LSV) of various 7% AMC substituted LFO photocathodes and as a function Ba^{2+} content recorded at 5 mV s^{-1} in O_2-saturated 0.1M Na_2SO_4 aqueous solution at pH 12, under a square wave 405 nm light perturbation and a photon flux of 3.25×10^{15} cm^{-2} s^{-1}. The responses for all AMC substituted films are significantly higher than for pristine LFO, with all showing a similar photocurrent-voltage dependence and an onset potential close to 1.2 V. Interestingly, **Figure 7b** shows that the photocurrent response as a function of the Ba^{2+} content goes through a maximum at around 7%. A similar trend is observed for all AMC, except Mg^{2+}, as shown in **Figure 7c** (LSV of the films as a function of AMC substitution levels can be found in **Figure S4**). Indeed, photocurrent responses show a weak increase upon increasing Mg^{2+} substitution up to 17%. We rationalise this behaviour in terms of the affinity of Mg^{2+} to the B-site of the perovskite lattice as predicted by Taylor et al.[45] Diez-Garcia and Gomez has also reported photocurrent enhancement in the presence of Mg^{2+}, although they only assume B-site substitution which is not entirely supported by our XPS observations.[27]

Figures 7d shows the external quantum efficiency (EQE) spectra of the pristine and 7% AMC substituted films in O_2-saturated 0.1M Na_2SO_4 aqueous solutions at pH 12. EQE values closed to 20% is obtained in the case of 7% Ba^{2+} substituted at a wavelength close to 360 nm and potential bias of 0.45 V vs RHE, which is one of the highest EQE value reported for LFO photocathodes. Linear sweep voltammetry carried out under the same conditions as in **Figure 7a** but after 1 hr of continuous illumination and after 45 days show identical trends and values, confirming the strong chemical stability of these films (**Figure S4**). Tauc plots constructed from EQE data (**Figure 7e**) clearly demonstrate that charge carriers are only generated upon excitation above 2.72 eV, which we have identified as the effective bandgap of the material (**Figure 4b**). This observation is in contrast with the Wheeler et al. study, which concluded that photocurrent enhancement upon K^+ substitution is linked to a decrease in the bandgap conclusion.[26]
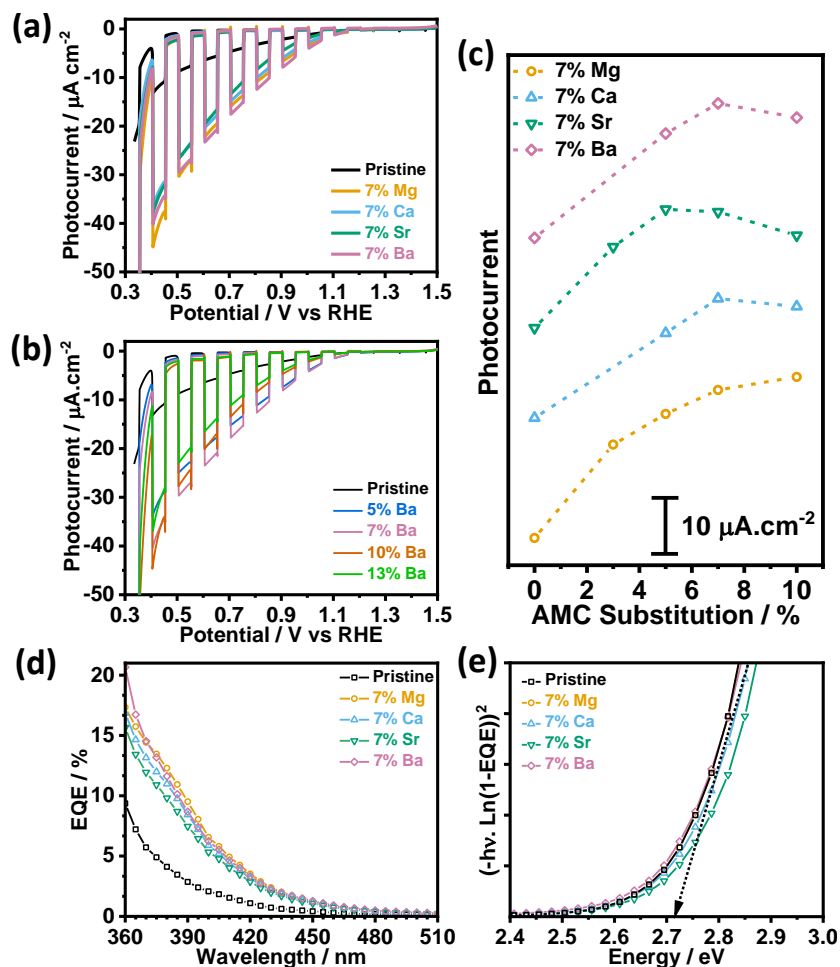
Figure 7. Photoelectrochemical responses in O_2-saturated 0.1M Na_2SO_4 aqueous solution pH 12: (a-b) 5 mV s^{-1} linear sweep voltammetry under a square wave 405 nm light perturbation and photon flux of 3.25×10^{15} cm^{-2} s^{-1}; (c) Photocurrent response at 0.45 V vs RHE as a function of the type and extent of AMC substitution; (d) External quantum efficiency spectra for the pristine and 7% AMC substituted thin films; (e) Tauc plot representation of the EQE demonstrating that charge carriers are generated only above the 2.72 eV edge for all LFO thin films. Photocurrent transients for different substitution levels of Mg^{2+}, Sr^{2+} and Ca^{2+} are shown in **Figure S4**.

To rationalise the photocurrent enhancement mechanism, we explore the behaviour in Ar-saturated solution as displayed in **Figure 8**. LSV curves for all 7% AMC substituted films (**Figure 8a**) and as a function of Ba^{2+} content (**Figure 8b**) were recorded under the same conditions as in **Figure 7a** and **7b** after purging the solution with Ar for over 30 min. In all cases, a significant improvement in the magnitude of the photoresponses is observed, although there is clear evidence of fast surface recombination. Indeed, there is a sharp increase in the initial photocurrent (displacement current) followed by a substantial relaxation to a low quasi-stationary photocurrent. The off-transient is a positive photocurrent overshot and a relaxation with a similar time constant, which is clearly illustrated in **Figure S6**. This behaviour is somewhat different from those observed in pristine highly crystalline LFO nanoparticle thin-films, which are characterised by a highly asymmetric photocurrent transient responses associated with hindered minority carrier transfer rather than surface

recombination.[15,17] Consequently, AMC substitution has a strong effect on carrier mobility leading to high displacement current, but also promotes surface carrier recombination in Ar-saturated solution.
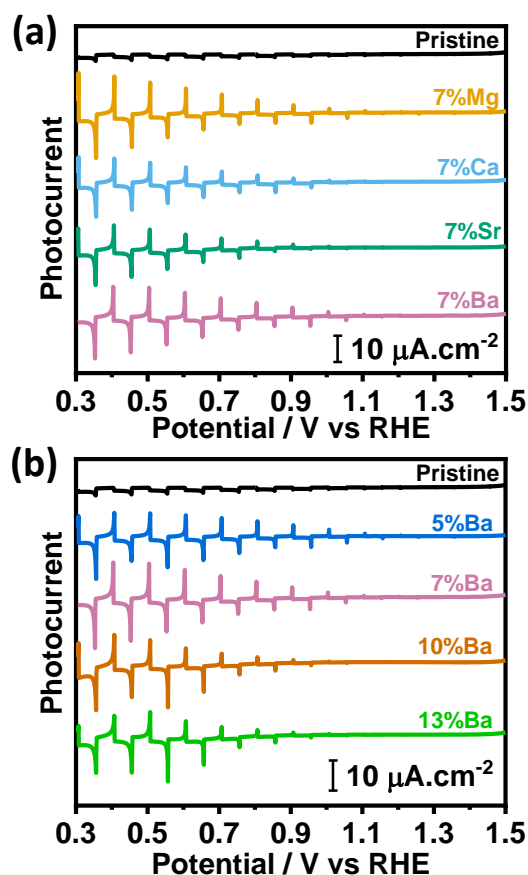

Figure 8. Transient photocurrent responses in Ar-saturated 0.1M Na_2SO_4 aqueous solution pH 12 of (a) pristine LFO thin films and 7% AMC substituted, and (b) for different extents of Ba substituted LFO films. Transients were recorded at 5 mV s^{-1} linear sweep voltammetry and square wave light perturbation (405 nm and 3.25×10^{15} cm^{-2} s^{-1} photon flux). Photocurrent transients of LFO films with different substitution levels of Mg^{2+}, Sr^{2+} and Ca^{2+} are shown in **Figure S5**.

The role of sub-bandgap states in photoelectrochemical responses. The effect of AMC substitution in electronic states near the valence band can be schematically illustrated in **Figure 9**, showing the dampening of intrinsic A-states and the emergence of B-states. With regards to A-states, these are located close to the valence band, remaining fully populated across most of the potential range investigated. These states behave as hole-traps, slowing down the transport of the majority carriers. This can be observed in the normalised photocurrent transients shown in **Figure S6**, where the photocurrent rise time in the on-transient and decay in the off-transient are slower in pristine LFO than AMC substituted LFO films. As demonstrated by Zhang et al., surface states probed electrochemically act as majority carriers trap states, leading to transient photocurrent responses significantly slower than the RC time constant.[46] Consequently, the dampening of A-states upon AMC

substitution is responsible for the sharpening of instantaneous (displacement) photocurrent shown in **Figure S6**.

The enhancement of the photocurrent responses towards oxygen reduction is not only associated with an improvement in majority carrier transport (dampening of A-states) but crucially with increasing kinetics of electron transfer assisted via B-states. The Gerischer formalism for electron transfer is based on the isoelectronic nature of the interfacial process, i.e. heterogeneous electron transfer involves density of states in the solid and the redox species located at the same energy.[47–50] As shown in **Figure 9**, B-states are located close to the standard oxygen redox energy; therefore, these states can mediate electron transfer from LFO. This is supported by the substantial increase in dark current in O_2 saturated solutions upon AMC substitution, as shown in **Figure S7**. Indeed, our previous works have shown that O_2 reduction kinetics at perovskite oxides are strongly linked to the density of states in the potential range between 0.5 and 1.2 V vs RHE.[30,51] The data show a systematic increase in the dark current at potentials more negative than 0.8 V vs RHE, i.e. once the density of B-states is fully populated. Under illumination, B-states are populated at all potentials accelerating the oxygen reduction kinetics (photocurrent).
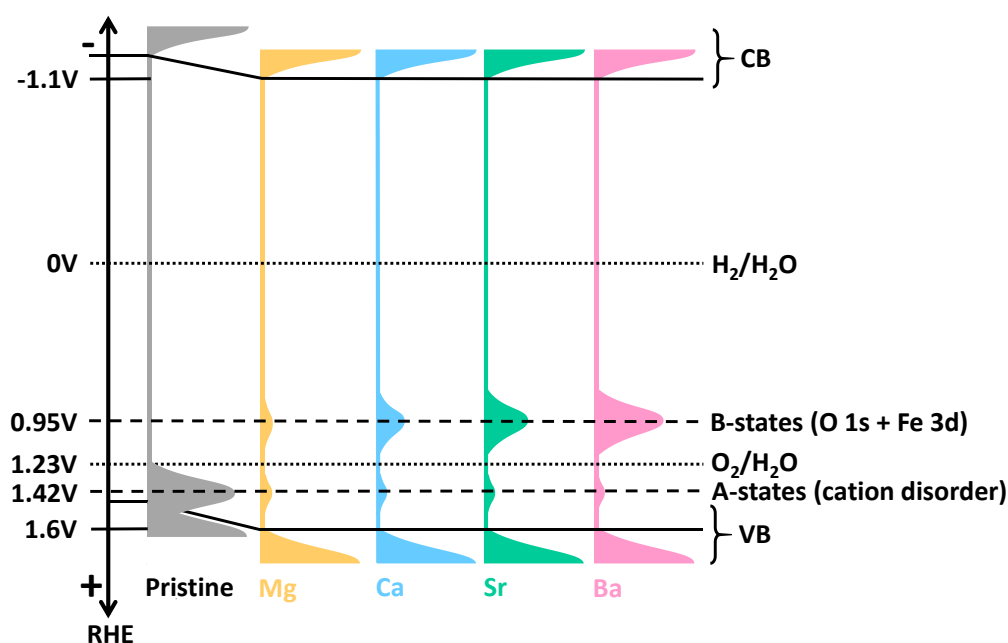
Figure 9. Schematic representation of the position of valence band edge as well as of the hydrated A- and B-states for pristine and AMC substituted LFO thin films. A-states are linked to intrinsic defects linked to cation disorder, while B-states are a combination of O 1s and Fe 3d states associated with high Fe-oxidation states.

The role of the sub-bandgap states in the photoelectrochemical hydrogen evolution reaction is somewhat less clear. We could postulate that in the absence of O_2, B-states can act as recombination centres as the charge transfer kinetics will be nominally zero. However, surface recombination can also occur in sub-band-gaps states closer to the conduction band edge, which is inaccessible to electrochemical experiments (e.g. oxygen vacancies). In this respect, it is important to raise a note of

caution on rationalising experimental trends employing DFT based electronic structure calculations. Most studies reporting changes in electronic structures as a result of cation substitution correlate their findings with optimised stoichiometric structures, disregarding the variety of intrinsic defects present in these complex materials (particularly those synthesised under O_2-rich environment).[26,40] Consequently, our understanding of electronic states associated with extrinsic and intrinsic defect structures remain rather shallow. Our study only provides a partial picture into these complex issues which are crucial to our understanding of this class of high-correlated electron systems in electrocatalysis, photocatalysis and artificial photosynthesis.

CONCLUSION

Divalent alkaline-earth metal cations (AMC) Mg^{2+}, Ca^{2+}, Sr^{2+} and Ba^{2+} substitution into $LaFeO_3$ thin-films prepared by sol-gel methods leads to changes in the electronic structure close to the valence band edge with a strong impact in photoelectrochemical performance. XRD and XPS analysis reveal a complex picture where parameters such lattice constant and covalency are affected by the type and extent of AMC substitution. At very low substitution levels (below 5%), sites featuring higher Fe oxidation states promote the contraction of the lattice constant, which is partially compensated at higher substitution levels by strain effects arising from the larger AMC. XPS analysis reveals a linear correlation between the BE of Fe $2p_{3/2}$ and O 1s associated with the perovskite lattice, suggesting that the Fe oxidation state and covalency of the Fe-O bond are strongly correlated regardless of the AMC nature. The structural and electronic effects of AMC substitution also confirm that substitution takes place at the A-site, except for Mg^{2+}, which can also occupy B-sites.

The structural and electronic changes promoted by AMC substitution are probed by current-voltage curves and electrochemical impedance spectroscopy in alkaline solutions. Pristine LFO films exhibit states located around 100 to 200 meV above the valence band edge (A-states), which are linked to intrinsic defects such as cation vacancies. AMC substitution attenuates these states (while substantially increasing the density of majority carriers), as well as promoting deeper states centred at 600 meV above the valence band edge (B-states). Dynamic photoelectrochemical studies show that A-states acts as hole-traps, decreasing the mobility of charge carriers. On the other hand, B-states promotes the photoelectrochemical reduction of oxygen. In the absence of oxygen, AMC substitution increases in the displacement (transient) photocurrent but the photostationary values are strongly affected by surface recombination. Currently, it remains to be fully elucidated whether surface recombination occurs at B-states or higher sub-bandgap states under oxygen-free solutions. These observations strongly point forwards to a significant improvement of LFO as photocatalysts for water remediation upon AMC substitution below 10%. With regards to photoelectrochemical hydrogen generation, new approaches are required in order to minimise intrinsic hole-trap states while promoting density of states near the conduction band, which can facilitate interfacial electron transfer.

ACKNOWLEDGEMENT

ASSOCIATED CONTENT

SUPPORTING INFORMATION

The Supporting Information is available free of charge on the ACS Publication website at DOI: xxx

Figure S1. Topography and composition of alkaline-earth metal cation (AMC) substituted $LaFeO_3$ (LFO).

Figure S2. XRD analysis of AMC substituted $LaFeO_3$ (LFO).

Figure S3. Deconvolution of La 3d, Fe 2p, O 1s XPS bands of 7% Sr substituted LFO thin-film.

Figure S4. Photoelectrochemical responses of AMC substituted LFO in the presence of O_2.

Figure S5. Photoelectrochemical responses of AMC substituted LFO under O_2 free conditions.

Figure S6. Dynamic photocurrent transient responses of pristine and 7% Ba substituted LFO.

Figure S7. Oxygen reduction reaction in the dark as a function of Ba^{2+} content.

AUTHOR INFORMATION

*CORRESPONDING AUTHORS

Email: devendra.tiwari@northumbria.ac.uk; Telephone +44 191 227 4616

Email: david.fermin@bristol.ac.uk; Telephone +44 117 9288981

ORCID

David Fermin: 0000-0002-0376-5506

Devendra Tiwari: 0000-0001-8225-0000

PRESENT ADDRESS

†Current affiliation: Department of Mathematics, Physics & Electrical Engineering, Northumbria University, Ellison Place, Newcastle upon Tyne NE1 8ST, UK

AUTHOR CONTRIBUTIONS

XS prepared and conducted all experiments reported. DT performed and analysed electrochemical impedance spectroscopy and XPS spectral deconvolution. All authors contributed to the data analysis and preparation of the manuscript. DT and DJF supervised the entire programme.

NOTES: The authors declare no competing financial interest.

REFERENCES

(1)   Lee, D. K.; Lee, D.; Lumley, M. A.; Choi, K. S. Progress on Ternary Oxide-Based Photoanodes for Use in Photoelectrochemical Cells for Solar Water Splitting. *Chem. Soc. Rev.* **2019**, *48*, 2126–2157.

(2)   Hwang, J.; Rao, R. R.; Giordano, L.; Katayama, Y.; Yu, Y.; Shao-Horn, Y. Perovskites in Catalysis and Electrocatalysis. *Science* **2017**, *358*, 751–756.

(3)   Yang, C.; Wang, Z.; Lin, T.; Yin, H.; Lü, X.; Wan, D.; Xu, T.; Zheng, C.; Lin, J.; Huang, F.; Xie, X.; Jiang, M. Core-Shell Nanostructured "Black" Rutile Titania as Excellent Catalyst for Hydrogen Production Enhanced by Sulfur Doping. *J. Am. Chem. Soc.* **2013**, *135*, 17831–17838.

(4)   Liao, A.; He, H.; Tang, L.; Li, Y.; Zhang, J.; Chen, J.; Chen, L.; Zhang, C.; Zhou, Y.; Zou, Z. Quasi-Topotactic Transformation of FeOOH Nanorods to Robust Fe_2O_3 Porous Nanopillars Triggered with a Facile Rapid Dehydration Strategy for Efficient Photoelectrochemical Water Splitting. *ACS Appl. Mater. Interfaces* **2018**, *10*, 10141–10146.

(5)   Kment, S.; Riboni, F.; Pausova, S.; Wang, L.; Wang, L.; Han, H.; Hubicka, Z.; Krysa, J.; Schmuki, P.; Zboril, R. Photoanodes Based on TiO_2 and α-Fe_2O_3 for Solar Water Splitting-Superior Role of 1D Nanoarchitectures and of Combined Heterostructures. *Chem. Soc. Rev.* **2017**, *46*, 3716–3769.

(6)   Kim, T. W.; Ping, Y.; Galli, G. A.; Choi, K. S. Simultaneous Enhancements in Photon Absorption and Charge Transport of Bismuth Vanadate Photoanodes for Solar Water Splitting. *Nat. Commun.* **2015**, *6*, 1–10.

(7)   Lee, D. K.; Choi, K. S. Enhancing Long-Term Photostability of $BiVO_4$ Photoanodes for Solar Water Splitting by Tuning Electrolyte Composition. *Nat. Energy* **2018**, *3*, 53–60.

(8)   Kim, J. H.; Lee, J. S. Elaborately Modified $BiVO_4$ Photoanodes for Solar Water Splitting. *Adv. Mater.* **2019**, *31*, 1–35.

(9)   Paracchino, A.; Mathews, N.; Hisatomi, T.; Stefik, M.; Tilley, S. D.; Grätzel, M. Ultrathin Films on Copper(I) Oxide Water Splitting Photocathodes: A Study on Performance and Stability. *Energy Environ. Sci.* **2012**, *5*, 8673–8681.

(10)   Kang, D.; Hill, J. C.; Park, Y.; Choi, K. S. Photoelectrochemical Properties and Photostabilities of High Surface Area $CuBi_2O_4$ and Ag-Doped $CuBi_2O_4$ Photocathodes. *Chem. Mater.* **2016**, *28*, 4331–4340.

(11)   Berglund, S. P.; Abdi, F. F.; Bogdanoff, P.; Chemseddine, A.; Friedrich, D.; Van De Krol, R. Comprehensive Evaluation of $CuBi_2O_4$ as a Photocathode Material for Photoelectrochemical Water Splitting. *Chem. Mater.* **2016**, *28*, 4231–4242.

(12)   Hu, S.; Shaner, M. R.; Beardslee, J. A.; Lichterman, M.; Brunschwig, B. S.; Lewis, N. S. Amorphous TiO_2 Coatings Stabilize Si, GaAs, and GaP Photoanodes for Efficient Water Oxidation. *Science* **2014**, *344*, 1005–1009.

(13)   Aguirre, M. E.; Zhou, R.; Eugene, A. J.; Guzman, M. I.; Grela, M. A. Cu_2O/TiO_2 Heterostructures for CO_2 Reduction through a Direct Z-Scheme: Protecting Cu_2O from Photocorrosion. *Appl. Catal. B Environ.* **2017**, *217*, 485–493.

(14)   Nunez, P.; Richter, M. H.; Piercy, B. D.; Roske, C. W.; Cabán-Acevedo, M.; Losego, M. D.; Konezny, S. J.; Fermin, D. J.; Hu, S.; Brunschwig, B. S.; Lewis, N. S. Characterization of Electronic Transport through Amorphous TiO_2 Produced by Atomic Layer Deposition. *J. Phys. Chem. C* **2019**, *123*, 20116–20129.

(15)   Sun, X.; Tiwari, D.; Fermin, D. J. Nanostructured LaFeO$_3$ Photocathodes with Onset Potentials for the Hydrogen Evolution Reaction Over 1.4 V vs. RHE. *J. Electrochem. Soc.* **2019**, *166*, H764–H768.

(16)   Wheeler, G. P.; Choi, K. S. Photoelectrochemical Properties and Stability of Nanoporous P-Type LaFeO$_3$ Photoelectrodes Prepared by Electrodeposition. *ACS Energy Lett.* **2017**, *2*, 2378–2382.

(17)   Celorrio, V.; Bradley, K.; Weber, O. J.; Hall, S. R.; Fermín, D. J. Photoelectrochemical Properties of LaFeO$_3$ Nanoparticles. *ChemElectroChem* **2014**, *1*, 1667–1671.

(18)   Díez-García, M. I.; Celorrio, V.; Calvillo, L.; Tiwari, D.; Gómez, R.; Fermín, D. J. YFeO$_3$ Photocathodes for Hydrogen Evolution. *Electrochim. Acta* **2017**, *246*, 365–371.

(19)   Radmilovic, A.; Smart, T. J.; Ping, Y.; Choi, K. S. Combined Experimental and Theoretical Investigations of N-Type BiFeO$_3$ for Use as a Photoanode in a Photoelectrochemical Cell. *Chem. Mater.* **2020**, *32*, 3262–3270.

(20)   Freeman, E.; Kumar, S.; Thomas, S. R.; Pickering, H.; Fermin, D. J.; Eslava, S. PrFeO$_3$ Photocathodes Prepared Through Spray Pyrolysis. *ChemElectroChem* **2020**, *7*, 1–9.

(21)   Prévot, M. S.; Guijarro, N.; Sivula, K. Enhancing the Performance of a Robust Sol-Gel-Processed p-Type Delafossite CuFeO$_2$ Photocathode for Solar Water Reduction. *ChemSusChem* **2015**, *8*, 1359–1367.

(22)   Díez-García, M. I.; Gómez, R. Investigating Water Splitting with CaFe$_2$O$_4$ Photocathodes by Electrochemical Impedance Spectroscopy. *ACS Appl. Mater. Interfaces* **2016**, *8*, 21387–21397.

(23)   Freeman, E.; Kumar, S.; Celorrio, V.; Park, M. S.; Kim, J. H.; Fermin, D. J.; Eslava, S. Strategies for the Deposition of LaFeO$_3$ Photocathodes: Improving the Photocurrent with a Polymer Template. *Sustain. Energy Fuels* **2020**, *4*, 884–894.

(24)   Pawar, G. S.; Tahir, A. A. Unbiased Spontaneous Solar Fuel Production Using Stable LaFeO$_3$ Photoelectrode. *Sci. Rep.* **2018**, *8*, 1–9.

(25)   Wang, P.; He, Y.; Mi, Y.; Zhu, J.; Zhang, F.; Liu, Y.; Yang, Y.; Chen, M.; Cao, D. Enhanced Photoelectrochemical Performance of LaFeO$_3$ Photocathode with Au Buffer Layer. *RSC Adv.* **2019**, *9*, 26780–26786.

(26)   Wheeler, G. P.; Baltazar, V. U.; Smart, T. J.; Radmilovic, A.; Ping, Y.; Choi, K. S. Combined Theoretical and Experimental Investigations of Atomic Doping to Enhance Photon Absorption and Carrier Transport of LaFeO$_3$ Photocathodes. *Chem. Mater.* **2019**, *31*, 5890–5899.

(27)   Díez-García, M. I.; Gómez, R. Metal Doping to Enhance the Photoelectrochemical Behavior of LaFeO$_3$ Photocathodes. *ChemSusChem* **2017**, *10*, 2457–2463.

(28)   Hayashi, N.; Yamamoto, T.; Kageyama, H.; Nishi, M.; Watanabe, Y.; Kawakami, T.; Matsushita, Y.; Fujimori, A.; Takano, M. BaFeO$_3$: A Ferromagnetic Iron Oxide. *Angew. Chemie - Int. Ed.* **2011**, *50*, 12547–12550.

(29)   Celorrio, V.; Calvillo, L.; van den Bosch, C. A. M.; Granozzi, G.; Aguadero, A.; Russell, A. E.; Fermín, D. J. Mean Intrinsic Activity of Single Mn Sites at LaMnO$_3$ Nanoparticles Towards the Oxygen Reduction Reaction. *ChemElectroChem* **2018**, *5*, 3044–3051.

(30)   Celorrio, V.; Calvillo, L.; Dann, E.; Granozzi, G.; Aguadero, A.; Kramer, D.; Russell, A. E.; Fermín, D. J. Oxygen Reduction Reaction at La$_x$Ca$_{1-x}$MnO$_3$ Nanostructures: Interplay between A-Site Segregation and B-Site Valency. *Catal. Sci. Technol.* **2016**, *6*, 7231–7238.

(31) Celorrio, V.; Calvillo, L.; Granozzi, G.; Russell, A. E.; Fermin, D. J. $AMnO_3$ (A = Sr, La, Ca, Y) Perovskite Oxides as Oxygen Reduction Electrocatalysts. *Top. Catal.* **2018**, *61*, 154–161.

(32) Wang, L.; Du, Y.; Sushko, P. V.; Bowden, M. E.; Stoerzinger, K. A.; Heald, S. M.; Scafetta, M. D.; Kaspar, T. C.; Chambers, S. A. Hole-Induced Electronic and Optical Transitions in $La_{1-x}Sr_xFeO_3$ Epitaxial Thin Films. *Phys. Rev. Mater.* **2019**, *3*, 1–8.

(33) Grosvenor, A. P.; Kobe, B. A.; Biesinger, M. C.; McIntyre, N. S. Investigation of Multiplet Splitting of Fe 2p XPS Spectra and Bonding in Iron Compounds. *Surf. Interface Anal.* **2004**, *36*, 1564–1574.

(34) Brundle, C. R.; Chuang, T. J.; Wandelt, K. Core and Valence Level Photoemission Studies of Iron Oxide Surfaces and the Oxidation of Iron. *Surf. Sci.* **1977**, *68*, 459–468.

(35) She, S.; Yu, J.; Tang, W.; Zhu, Y.; Chen, Y.; Sunarso, J.; Zhou, W.; Shao, Z. Systematic Study of Oxygen Evolution Activity and Stability on $La_{1-x}Sr_xFeO_{3-\delta}$ Perovskite Electrocatalysts in Alkaline Media. *ACS Appl. Mater. Interfaces* **2018**, *10*, 11715–11721.

(36) Zhu, Y.; Zhou, W.; Yu, J.; Chen, Y.; Liu, M.; Shao, Z. Enhancing Electrocatalytic Activity of Perovskite Oxides by Tuning Cation Deficiency for Oxygen Reduction and Evolution Reactions. *Chem. Mater.* **2016**, *28*, 1691–1697.

(37) Hu, S.; Zhang, L.; Liu, H.; Cao, Z.; Yu, W.; Zhu, X.; Yang, W. Alkaline-Earth Elements (Ca, Sr and Ba) Doped $LaFeO_{3-\delta}$ Cathodes for CO_2 Electroreduction. *J. Power Sources* **2019**, *443*, 1–10.

(38) Shi, C.; Qin, H.; Zhao, M.; Wang, X.; Li, L.; Hu, J. Investigation on Electrical Transport, CO Sensing Characteristics and Mechanism for Nanocrystalline $La_{1-x}Ca_xFeO_3$ Sensors. *Sensors Actuators, B Chem.* **2014**, *190*, 25–31.

(39) Bocquet, A. E.; Fujimori, A.; Mizokawa, T.; Saitoh, T.; Namatame, H.; Suga, S.; Kimizuka, N.; Takeda, Y.; Takano, M. Electronic Structure of $SrFe^{4+}O_3$ and Related Fe Perovskite Oxides. *Phys. Rev. B* **1992**, *45*, 1561–1570.

(40) Shen, Z.; Zhuang, Y.; Li, W.; Huang, X.; Oropeza, F. E.; Hensen, E. J. M.; Hofmann, J. P.; Cui, M.; Tadich, A.; Qi, D.; Cheng, J.; Li, J.; Zhang, K. H. L. Increased Activity in the Oxygen Evolution Reaction by Fe^{4+}-Induced Hole States in Perovskite $La_{1-x}Sr_xFeO_3$. *J. Mater. Chem. A* **2020**, *8*, 4407–4415.

(41) Ritzmann, A. M.; Muñoz-García, A. B.; Pavone, M.; Keith, J. A.; Carter, E. A. Ab Initio DFT+U Analysis of Oxygen Vacancy Formation and Migration in $La_{1-x}Sr_xFeO_{3-\delta}$ (x = 0, 0.25, 0.50). *Chem. Mater.* **2013**, *25*, 3011–3019.

(42) Taylor, F. H.; Buckeridge, J.; Catlow, C. R. A. Defects and Oxide Ion Migration in the Solid Oxide Fuel Cell Cathode Material $LaFeO_3$. *Chem. Mater.* **2016**, *28*, 8210–8220.

(43) Stoerzinger, K. A.; Wang, L.; Ye, Y.; Bowden, M.; Crumlin, E. J.; Du, Y.; Chambers, S. A. Linking Surface Chemistry to Photovoltage in Sr-Substituted $LaFeO_3$ for Water Oxidation. *J. Mater. Chem. A* **2018**, *6*, 22170–22178.

(44) Acharya, S.; Mondal, J.; Ghosh, S.; Roy, S. K.; Chakrabarti, P. K. Multiferroic Behavior of Lanthanum Orthoferrite ($LaFeO_3$). *Mater. Lett.* **2010**, *64*, 415–418.

(45) Taylor, F. H.; Buckeridge, J.; Catlow, C. R. A. Screening Divalent Metals for A- and B-Site Dopants in $LaFeO_3$. *Chem. Mater.* **2017**, *29*, 8147–8157.

(46) Zhang, Q.; Celorrio, V.; Bradley, K.; Eisner, F.; Cherns, D.; Yan, W.; Fermín, D. J. Density of Deep Trap States in Oriented TiO_2 Nanotube Arrays. *J. Phys. Chem. C* **2014**, *118*, 18207–18213.

(47)   Gerischer, H. Über Den Ablauf von Redoxreaktionen an Metallen Und an Halbleitern: I. Allgemeines Zum Elektronenübergang Zwischen Einem Festkörper Und Einem Redoxelektrolyten. *Zeitschrift fur Phys. Chemie* **1960**, *26*, 223–247.

(48)   Gerischer, H. Über Den Ablauf Von Redoxreaktionen an Metallen Und an Halbleitern III. Halbleiterelektroden. *Zeitschrift fur Phys. Chemie* **1961**, *27*, 48–79.

(49)   In Advances in Electrochemistry and Electrochemical Engineering: Volume 1: Electrochemistry, 1st ed. 1961.; Delahay, P., Ed.; Wiley Interscience: New York, 1961.

(50)   Kissling, G. P.; Bünzli, C.; Fermín, D. J. Tuning Electrochemical Rectification via Quantum Dot Assemblies. *J. Am. Chem. Soc.* **2010**, *132*, 16855–16861.

(51)   Celorrio, V.; Dann, E.; Calvillo, L.; Morgan, D. J.; Hall, S. R.; Fermin, D. J. Oxygen Reduction at Carbon-Supported Lanthanides: The Role of the B-Site. *ChemElectroChem* **2016**, *3*, 283–291.

TOC

Alkaline-earth metal substitution in LaFeO$_3$

Correlated
Fe-state & Fe-O covalency

Trap states & Catalytic sites